

High Frequency MoS₂ Nanomechanical Resonators

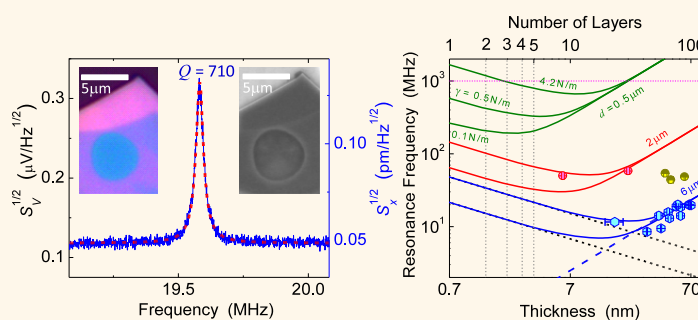
Jaesung Lee,^{†,‡} Zenghui Wang,^{†,‡} Keliang He,[§] Jie Shan,[§] and Philip X.-L. Feng^{†,*}

Departments of [†]Electrical Engineering and Computer Science and [§]Physics, Case Western Reserve University, 10900 Euclid Avenue, Cleveland, Ohio 44106, United States. [†]These authors contributed equally.

ABSTRACT Molybdenum disulfide (MoS₂), a layered semiconducting material in transition metal dichalcogenides (TMDCs), as thin as a monolayer (consisting of a hexagonal plane of Mo atoms covalently bonded and sandwiched between two planes of S atoms, in a trigonal prismatic structure), has demonstrated unique properties and strong promises for emerging two-dimensional (2D) nanodevices. Here we report on the demonstration of movable and vibrating MoS₂ nanodevices, where MoS₂ diaphragms as thin

as 6 nm (a stack of 9 monolayers) exhibit fundamental-mode nanomechanical resonances up to $f_0 \sim 60$ MHz in the very high frequency (VHF) band, and frequency-quality (Q) factor products up to $f_0 \times Q \sim 2 \times 10^{10}$ Hz, all at room temperature. The experimental results from many devices with a wide range of thicknesses and lateral sizes, in combination with theoretical analysis, quantitatively elucidate the elastic transition regimes in these ultrathin MoS₂ nanomechanical resonators. We further delineate a roadmap for scaling MoS₂ 2D resonators and transducers toward microwave frequencies. This study also opens up possibilities for new classes of vibratory devices to exploit strain- and dynamics-engineered ultrathin semiconducting 2D crystals.

KEYWORDS: two-dimensional (2D) crystals · molybdenum disulfide (MoS₂) · nanoelectromechanical systems (NEMS) · resonators · thermomechanical noise · frequency scaling · displacement sensitivity



Actuating and sensing at the nano-scale are among the most important yet challenging functions in realizing new tools to interact with ultrasmall objects of interest. Such actuating and sensing functions often require harnessing mechanical degrees of freedom and exquisitely motion-coupled properties in nanostructures. Nanoelectromechanical systems (NEMS) based on atomically thin, two-dimensional (2D) crystals, such as graphene,^{1–5} have recently shown attractive potential for novel actuators and sensors, owing to the ultralow weight and ultrahigh mechanical flexibility of these materials and other 2D attributes that are inaccessible in bulk.^{1–7} While graphene, the early hallmark of 2D crystals, has been extensively studied for NEMS,^{1–5} such explorations in 2D crystals beyond graphene with distinct electronic and optical properties are highly desirable.

Ultrathin crystals of transition metal dichalcogenides (TMDCs)^{8,9} have emerged as a new class of 2D layered materials beyond graphene. Molybdenum disulfide (MoS₂),

a prototype semiconducting TMDC, with a sizable bandgap and unique valley and spin properties,^{10–13} has demonstrated remarkable promise for new electronic and optoelectronic applications.^{8–17} In contrast to graphene being a semimetal, MoS₂ is a semiconductor with its electronic structure dependent on thickness and continuously on strain, as demonstrated experimentally.^{10,11,18} 2D MoS₂ crystals also offer excellent mechanical properties,^{18–20} similar to those of graphene.^{1–7} In addition to its ultralow weight (areal density of $\rho_A = 3.3 \text{ fg}/\mu\text{m}^2$ for monolayer), 2D MoS₂ has exceptional strain limit ($\epsilon_{\text{int}} \sim 10\text{--}20\%$)^{18,19} and high elastic modulus ($E_Y \sim 0.2\text{--}0.3 \text{ TPa}$).^{19,20} These properties suggest intriguing possibilities for innovating NEMS transducers where the mechanical properties of 2D MoS₂ are coupled to its band structure and other electronic and optoelectronic attributes (unavailable in graphene). However, motion-coupled MoS₂ nanodevices have not yet been explored, due to the difficulties not only in nanofabrication of movable

* Address correspondence to philip.feng@case.edu.

Received for review April 17, 2013 and accepted June 5, 2013.

Published online June 05, 2013
10.1021/nn4018872

© 2013 American Chemical Society

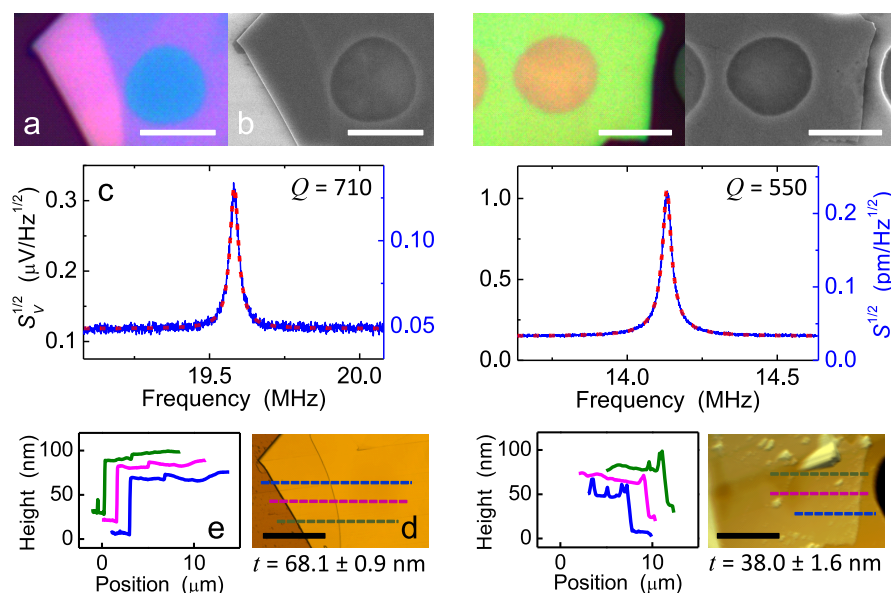


Figure 1. High frequency (HF) MoS₂ nanomechanical resonators and device characteristics. The left and right panels show data from two representative devices with different thicknesses. Shown in the same order within both panels: (a) Optical image; (b) SEM image; (c) Measured thermomechanical resonance (solid curve) and fit to a finite-Q harmonic resonator model (dashed curve); (d) AFM image (dashed lines indicate the approximate positions of height measurement traces); (e) Representative height measurement traces (offset for clarity), with colors corresponding to the dashed lines in (d). All scale bars are 5 μm .

devices, but also in detection of their vanishingly miniscule motions. In this work, we demonstrate MoS₂ NEMS resonators with resonances in the high and very high frequency (HF and VHF) bands, achieving displacement sensitivity of 30.2 fm/Hz^{1/2}, and with fundamental-mode frequency-quality factor product up to $f_0 \times Q \approx 2 \times 10^{10}$ Hz, a figure of merit that surpasses values in graphene NEMS counterparts.^{1–5} Combining experiment and analysis, we illustrate the important elastic regimes with scaling laws, which shed light on design and engineering of future devices toward microwave frequencies.

RESULTS AND DISCUSSION

Device Processing, Characterization, and Thermomechanical Resonance Measurement. We employ photolithography, wet etching, and micromechanical exfoliation to fabricate our prototype MoS₂ NEMS, which consist of exfoliated MoS₂ nanosheets covering predefined micro-trenches on a SiO₂-on-Si substrate (see Methods). The thickness of each suspended MoS₂ diaphragm is initially estimated by examining its color and contrast in optical microscope. After all the resonance measurements that we describe below, the thickness and surface of each device is carefully examined using atomic force microscopy (AFM) and scanning electron microscopy (SEM).

Without external excitations, thermal fluctuation and dissipation processes dictate the devices to be in Brownian motions, manifested as thermomechanical modes of damped harmonic resonators, each with a frequency-domain displacement spectral density (see Supporting Information, S1)

$$S_{x,th}^{1/2}(\omega) = \left(\frac{4k_B T \omega_0}{M_{\text{eff}} Q} \cdot \frac{1}{(\omega^2 - \omega_0^2)^2 + \omega^2 \omega_0^2 / Q^2} \right)^{1/2} \quad (1)$$

Here k_B is the Boltzmann constant, M_{eff} , ω_0 , and Q are the effective mass, angular resonance frequency, and quality factor of the mode, respectively. Given the structure and shape of our devices, the fundamental mode of the out-of-plane thermomechanical motions is the most salient. Thermomechanical motions are the minimal levels of motions that can be possibly measured from the devices, and set a fundamental limit for detection. We employ a specially engineered optical interferometry scheme that efficiently transduces motion into a voltage signal, $S_{v,th}^{1/2}(\omega) = \mathcal{R}(\omega) S_{x,th}^{1/2}(\omega)$ with $\mathcal{R}(\omega)$ being the transduction responsivity and with best motion sensitivities at the level of ~ 30 fm/Hz^{1/2} (see Methods and Supporting Information, S1 and S6). This enables us to directly observe the intrinsic thermomechanical modes of the devices at room temperature, and for some devices, in both vacuum and ambient air.

High Frequency and Very High Frequency MoS₂ Nanomechanical Resonators. We first demonstrate high frequency nanomechanical resonators based on MoS₂ diaphragms of $d \sim 6 \mu\text{m}$ in diameter, with thickness in the range of $t \approx 13$ –68 nm (~ 20 –97 layers). The left panel in Figure 1 shows the characteristics measured from a diaphragm with $d \approx 5.7 \mu\text{m}$ and $t \approx 68.1$ nm. This device exhibits a fundamental mode resonance at $f_0 \equiv \omega_0/2\pi \approx 19.68$ MHz, with $Q \approx 710$ (Figure 1c) in moderate vacuum of pressure (p) ≈ 6 mTorr. This device makes an exquisite interferometric motion transducer with a displacement sensitivity (noise floor) of 49.5 fm/Hz^{1/2} (see Supporting Information, S1). AFM measurements (Figure 1d,e)

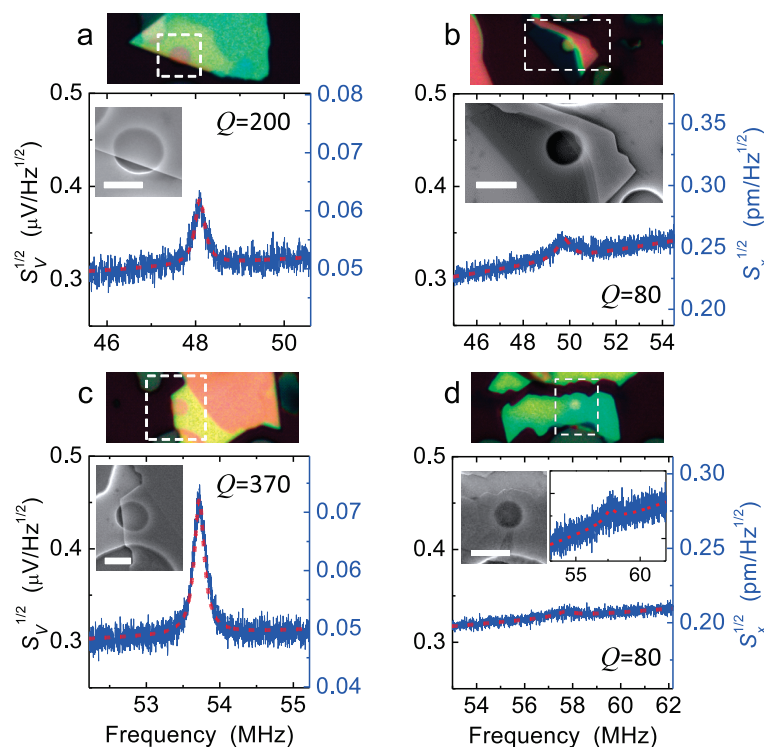


Figure 2. Very high frequency (VHF) thermomechanical resonances measured from smaller and thinner MoS₂ resonators. For each of the four devices, optical image, SEM image (corresponding to the dashed box in the optical image), and thermomechanical resonance are shown. The left axis denotes measured noise voltage spectral density, with the same scale in all four plots. The right axis is thermomechanical displacement spectral density, with individual scale depending on the characteristics of each device (thus, the interferometric transduction). Right inset in (d) is a zoom-in view of the same curve (rescaled the vertical axis). Device dimensions: (a) $d \approx 2.7 \mu\text{m}$, $t \approx 62.2 \text{ nm}$ (89 layers); (b) $1.9 \mu\text{m}$, 6.1 nm (9 layers); (c) $2.5 \mu\text{m}$, 43.0 nm (61 layers); (d) $1.5 \mu\text{m}$, 27.2 nm (39 layers). All scale bars are $2 \mu\text{m}$.

show thickness and surface morphological features. Right panel of Figure 1 shows data from a thinner device of similar size ($d \approx 5.5 \mu\text{m}$, $t \approx 38.0 \text{ nm}$, ~ 54 layers) with $f_0 \approx 14.13 \text{ MHz}$ and $Q \approx 550$, and a remarkable displacement sensitivity of $33.5 \text{ fm/Hz}^{1/2}$.

We further explore smaller, thinner devices and demonstrate MoS₂ resonators in the VHF (30–300 MHz) band (Figure 2). The thinnest device (Figure 2b), only 9-layer-thick (see Supporting Information, S2 for details), makes a VHF resonator with $f_0 \approx 49.7 \text{ MHz}$ and $Q \approx 80$. We further note that these MoS₂ resonators are very robust; even incompletely covered devices (Figure 2a,c) operate at VHF with considerably high quality factors (Qs). These smaller circular diaphragms all make excellent interferometric motion transducers with displacement resolutions down to ~ 40 – $250 \text{ fm/Hz}^{1/2}$ in the 30–60 MHz band.

We summarize in Figure 3a,b the characteristics, including both the resonance frequencies (f_0 values) and the Qs of all the devices investigated, with various dimensions. It is clear (Figure 3a) that smaller diameters lead to higher frequencies. In both groups, thicker devices tend to attain higher Qs (Figure 3b), suggesting surface-related dissipations ($Q^{-1} \propto 1/t$, or the surface-to-volume ratio, $S/V \sim 1/t$) in these devices. This is in excellent agreement with the well-known thickness-dependent Qs in conventional MEMS/NEMS resonators that have high surface-to-volume ratios.^{21,22}

We note that, in an earlier study on resonators made of graphene and very thin graphite,¹ no clear Q dependence on thickness was observed, which is in contrast with observations in this work and previous studies.^{21,22} It could be that the surface-related dissipation in those graphene/graphite resonators might have been overshadowed by other stronger damping effects. While there are considerable varieties of device sizes and thicknesses, we can use a widely adopted figure of merit (FOM), $f_0 \times Q$ product, to evaluate device performance and compare the MoS₂ resonators in this work with recent graphene resonators.^{1–5} The best FOM value achieved in our MoS₂ resonators is $f_0 \times Q \approx 2 \times 10^{10} \text{ Hz}$, which surpasses the highest $f_0 \times Q$ value in graphene devices reported to date, at room temperature and under similar experimental conditions.

We repeatedly observe that most of the thermomechanical resonances sustain even in ambient air. As shown in Figure 3d, Qs of ~ 500 – 100 in vacuum drop to $\sim 10^{-1}$ in air, following a power law of $Q \propto p^{-1/2}$ in the range of $p \sim 1$ – 100 Torr , and then $Q \propto p^{-1}$ in the range of $p \sim 100$ – 1000 Torr . These measured air damping (Q dependence on pressure) characteristics of MoS₂ resonators are similar to the Q -pressure dependence measured in other membrane-structured MEMS/NEMS resonators.²³ Data in all other plots are measured at $p \approx 6 \text{ mTorr}$ and therefore are not compromised by air damping. In Q data from vacuum in all devices, besides the visible correlation

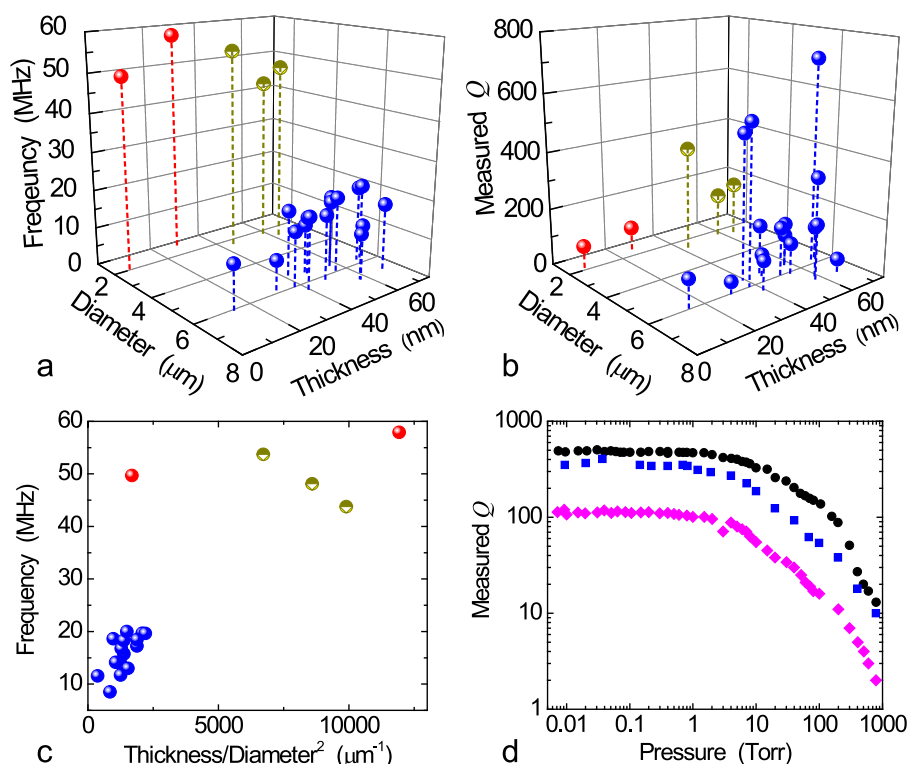


Figure 3. Performance of MoS₂ nanomechanical resonators. (a) Measured fundamental-mode resonance frequency, and (b) measured *Q* factor as functions of device dimensions. (c) Resonance frequency vs thickness over square of diameter (t/d^2). The blue and red symbols in a–c represent bigger and smaller devices, respectively. The divided-color symbols indicate devices based on incompletely covered microtrenches. (d) Measured *Q* dependence on pressure for different resonances. We have investigated >20 devices, see Supporting Information, S6, for a complete list of devices and their measured parameters.

to thickness (or $S/V \sim 1/t$), we observe no noticeable evidence suggesting dominant clamping losses (dependent on aspect ratio, *i.e.*, length-to-thickness or diameter-to-thickness ratio)^{24,25} or other mechanisms.

Theoretical Analysis of Elastic Transition Regime and Frequency Scaling. To gain insight and quantitative understandings of the device frequency scaling, we perform analytical modeling. For vibrations of clamped MoS₂ diaphragms with both flexural rigidity $D = E_v t^3 / [12(1 - \nu^2)]$ (ν being the Poisson ratio) and tension γ (N/m, as in surface tension), we determine the fundamental-mode resonance frequency to be^{26,27}

$$f_0 = \left(\frac{kd}{4\pi} \right) \sqrt{\frac{16D}{\rho d^4} \left[\left(\frac{kd}{2} \right)^2 + \frac{\gamma d^2}{4D} \right]} \quad (2)$$

where ρ is the areal mass density and k is a modal parameter that is determined numerically (see Supporting Information, S3). In the tension-dominant limit ($\gamma d^2/D \rightarrow \infty$), eq 2 converges into the membrane model, while in the modulus-dominant limit ($\gamma d^2/D \rightarrow 0$) it approaches the plate model. These asymptotic characteristics are clearly demonstrated in Figure 4, with scaling of f_0 upon varying device thickness. This leads to the *quantitative* determination of a “crossover” transition regime at intermediate thicknesses for any given diameter and tension level. Experimental data from

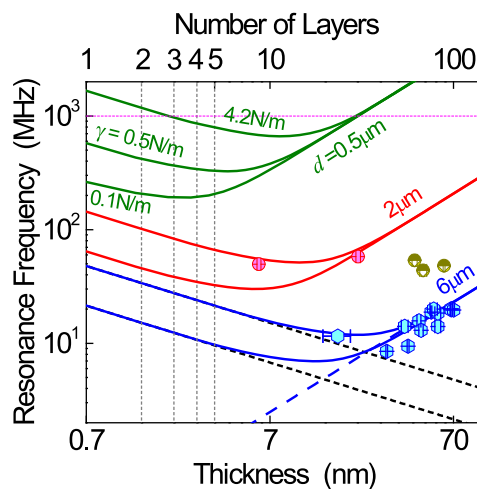


Figure 4. Elucidating elastic transition from the “plate” limit to the “membrane” limit in very thin MoS₂ resonators: (solid curves) calculated resonance frequency vs device thickness for three different device diameters, each with 0.1 and 0.5 N/m tension (except in the top curve family where we show an additional tension of 4.2 N/m, corresponding to 3% strain in monolayer); (black dashed lines) 6 μ m ideal membranes (eq S12) under 0.1 and 0.5 N/m tension; (blue dashed line) 6 μ m ideal plate (eq S13); (blue hexagons) measured devices with large diameter ($\sim 6 \mu$ m); (red circles) small diameter ($\sim 2 \mu$ m) devices. Circles with divided colors denote slightly larger ($\sim 2.5 \mu$ m) devices with less than complete coverage (as shown in Figure 2). Vertical dotted lines mark the thicknesses of 2–5 layers of MoS₂.

larger-diameter ($d \sim 6 \mu\text{m}$) devices agree well with the 6 μm curves, and data from smaller-diameter ($d \sim 2 \mu\text{m}$) devices match the 2 μm curves. Data from slightly larger ($d \sim 2.5 \mu\text{m}$) and incomplete diaphragms (see SEM images in Figure 2 for examples) fall in between the data from the above two groups.

Comparing our experimental and analytical results, we find that thicker devices essentially operate in the plate limit, where f_0 is determined by the device dimensions and shows little dependence on tension. This is also evident in Figure 3c where data from larger devices ($d \sim 6 \mu\text{m}$) appear to follow the trend of $f_0 \propto t/d^2$ for ideal plates. In contrast, our thinnest devices operate in the transition regime and approach the membrane limit. From these results we estimate a tension level of $\gamma \approx 0.3\text{--}0.5 \text{ N/m}$ in these devices, consistent with values obtained in static nanoindentation tests of mechanically exfoliated MoS_2 .^{19,20} This value is also comparable with that found in exfoliated graphene,⁶ suggesting similarity in the exfoliation processes of both materials. We note that these tension values correspond to strains of only $\varepsilon \approx 0.01\text{--}0.04\%$, which are $\sim 250\text{--}2000$ times lower than the intrinsic strain limit ($\sim 10\text{--}20\%$).^{18,19}

Our analysis indicates that ultrathin devices (e.g., below five monolayers, vertical dashed lines in Figure 4) will operate in the membrane limit and attain great tunability *via* tension. Importantly, here we clearly demonstrate that for $d \sim 2\text{--}6 \mu\text{m}$ or larger, devices thinner than 10–20 layers are already well in the membrane regime. For $d < 1 \mu\text{m}$, only few-layer devices behave as membranes. Figure 4 also provides the design guidelines and scaling laws: reducing the lateral dimension and engineering high tension are both effective toward scaling up the resonance frequency. For instance, for $d = 0.5 \mu\text{m}$ (the green curves in Figure 4), resonators with $f_0 = 1 \text{ GHz}$ can be achieved in both asymptotic regimes, by trading thickness *versus* tension. In particular, even a moderate tension of $\gamma \approx 4.2 \text{ N/m}$ (strain $\varepsilon \approx 1.5\%$ for bilayer and $\varepsilon \approx 3\%$ for

monolayer) leads to $f_0 > 1 \text{ GHz}$ for $d = 0.5 \mu\text{m}$ devices with less than three layers (Figure 4).

CONCLUSIONS

In conclusion, we have demonstrated a new type of nanomechanical resonators vibrating in the HF and VHF bands based on suspended 2D MoS_2 crystals. These MoS_2 devices demonstrate robust resonances with high Q s and naturally make motion transducers exhibiting exceptional displacement sensitivities approaching $30 \text{ fm/Hz}^{1/2}$ at room temperature. A figure of merit $f_0 \times Q \approx 2 \times 10^{10} \text{ Hz}$ is achieved at room temperature, among the highest in known nanomechanical resonators based on 2D materials including graphene. Our study unambiguously identifies the transition between the “plate” and “membrane” regimes and establishes quantitative design guidelines and scaling laws for engineering future generations of MoS_2 NEMS and ultrasensitive 2D resonant transducers. As thermomechanical fluctuations represent a fundamental noise floor, the thermomechanical resonant characteristics measured from the MoS_2 devices may provide important information for future engineering of MoS_2 resonant NEMS, where achieving large dynamic range²⁸ and matching to intrinsic noise floor are important. Examples include low-noise feedback oscillators,²⁹ noise thermometry,³⁰ and signal transduction near the quantum limit.³¹ Furthermore, the demonstration of very high frequency MoS_2 nanomechanical resonators with frequency scaling capability enables a 2D semiconducting NEMS platform for a number of exciting future experiments and device technologies, such as coupling dynamical strains and resonant motions into MoS_2 field effect transistors^{15–17} and optoelectronic devices,^{9,32} exploring spin interactions with MoS_2 NEMS resonators for quantum information processing,³³ and engineering vibratory and flexible devices toward fully exploiting the very high intrinsic strain limits^{18,19} promised by ultrathin MoS_2 structures.

METHODS

Device Fabrication. MoS_2 nanomechanical resonators are fabricated by exfoliating MoS_2 nanosheets onto prefabricated device structures. First, circular microtrenches of different sizes are patterned onto a silicon (Si) wafer covered with 290 nm of thermal oxide (SiO_2) using photolithography followed by buffered oxide etch (BOE). The etch time is chosen such that the flat Si surface is exposed. Then MoS_2 nanosheets are exfoliated onto this structured substrate. We note that the yield for making suspended MoS_2 devices with fully covered microtrenches is much lower than for making graphene devices with similar geometries, especially for thinner (mono- and few-layer) devices. Suspended MoS_2 sheets covering microtrenches are then identified under an optical microscope (Olympus MX50) with a $50\times$ objective, where all the optical images are taken.

Thermomechanical Resonance Measurement. Undriven Brownian motions of MoS_2 nanomechanical resonators are measured with a custom-built laser interferometry system (see Supporting Information, S1, for details). A He–Ne laser (632.8 nm) is focused

onto the suspended MoS_2 diaphragms using a $50\times$ microscope objective, with a spot size of $\sim 1 \mu\text{m}$. We apply a laser power of $\sim 100 \mu\text{W}\text{--}700 \mu\text{W}$ onto the device which assures good optical signal and does not exhibit measurable heating (see Supporting Information, S4). Optical interferometric readout of the MoS_2 device motion is accomplished by detecting the motion-modulated interference between the reflections from the MoS_2 diaphragm–vacuum interfaces and the underneath vacuum–Si interface. We have specially engineered our system to achieve $\text{pm/Hz}^{1/2}$ to $\text{fm/Hz}^{1/2}$ displacement sensitivities for various devices by exploiting latest advances and techniques in such schemes.^{34–36} The optical detection scheme and settings are carefully tuned to remain identical during the experiments. The vacuum chamber is maintained under moderate vacuum ($\sim 6 \text{ mTorr}$), except during characterization of air damping, when the pressure is regulated and varied between vacuum and atmospheric pressure (760 Torr). Throughout the pressure dependence measurements we observe no evidence of bulging effect due to trapped air underneath MoS_2 diaphragms

(see Supporting Information, S5). Thermomechanical noise spectral density is recorded with a spectrum analyzer (Agilent E4440A).

Scanning Electron Microscopy (SEM). SEM images are taken inside an FEI Nova NanoLab 200 field-emission SEM, using an Everhart-Thornley detector (ETD) for detecting secondary electrons at an acceleration voltage of 10 kV.

Atomic Force Microscopy (AFM). AFM images are taken with an Agilent N9610A AFM using tapping mode. To measure the thickness of each device, multiple traces are extracted from each scan, from which the thickness value and uncertainty are determined (see Supporting Information, S2).

Conflict of Interest: The authors declare no competing financial interest.

Acknowledgment. This work was supported by Case School of Engineering and the National Science Foundation (Grant No. DMR-0907477). We are also grateful to a T. Keith Glennan Fellowship and the Swagelok Center for Surface Analysis of Materials (SCSAM) at Case Western Reserve University.

Supporting Information Available: Additional technical details. This material is available free of charge via the Internet at <http://pubs.acs.org>.

REFERENCES AND NOTES

- Bunch, J. S.; van der Zande, A. M.; Verbridge, S. S.; Frank, I. M.; Tanenbaum, D. M.; Parpia, J. M.; Craighead, H. G.; McEuen, P. L. Electromechanical Resonators from Graphene Sheets. *Science* **2007**, *315*, 490–493.
- Chen, C. Y.; Rosenblatt, S.; Bolotin, K. I.; Kalb, W.; Kim, P.; Kymissis, I.; Stormer, H. L.; Heinz, T. F.; Hone, J. Performance of Monolayer Graphene Nanomechanical Resonators with Electrical Readout. *Nat. Nanotechnol.* **2009**, *4*, 861–867.
- van der Zande, A. M.; Barton, R. A.; Alden, J. S.; Ruiz-Vargas, C. S.; Whitney, W. S.; Pham, P. H. Q.; Park, J. W.; Parpia, J. M.; Craighead, H. G.; McEuen, P. L. Large-Scale Arrays of Single-Layer Graphene Resonators. *Nano Lett.* **2010**, *10*, 4869–4873.
- Eichler, A.; Moser, J.; Chaste, J.; Zdrojek, M.; Wilson-Rae, I.; Bachtold, A. Nonlinear Damping in Mechanical Resonators Made from Carbon Nanotubes and Graphene. *Nat. Nanotechnol.* **2011**, *6*, 339–342.
- Barton, R. A.; Parpia, J.; Craighead, H. G. Fabrication and Performance of Graphene Nanoelectromechanical Systems. *J. Vac. Sci. Technol., B* **2011**, *29*, 050801.
- Lee, C.; Wei, X.; Kysar, J. W.; Hone, J. Measurement of the Elastic Properties and Intrinsic Strength of Monolayer Graphene. *Science* **2008**, *321*, 385–388.
- Lee, C.; Li, Q. Y.; Kalb, W.; Liu, X.-Z.; Berger, H.; Carpick, R. W.; Hone, J. Frictional Characteristics of Atomically Thin Sheets. *Science* **2010**, *328*, 76–80.
- Novoselov, K. S.; Jiang, D.; Schedin, F.; Booth, T. J.; Khotkevich, V. V.; Morozov, S. V.; Geim, A. K. Two-Dimensional Atomic Crystals. *Proc. Natl. Acad. Sci. U.S.A.* **2005**, *102*, 10451–10453.
- Wang, Q. H.; Kalantar-Zadeh, K.; Kis, A.; Coleman, J. N.; Strano, M. S. Electronics and Optoelectronics of Two-Dimensional Transition Metal Dichalcogenides. *Nat. Nanotechnol.* **2012**, *7*, 699–712.
- Mak, K. F.; Lee, C.; Hone, J.; Shan, J.; Heinz, T. F. Atomically Thin MoS₂: A New Direct-Gap Semiconductor. *Phys. Rev. Lett.* **2010**, *105*, 136805.
- Splendiani, A.; Sun, L.; Zhang, Y. B.; Li, T. S.; Kim, J. H.; Chim, C.-Y.; Galli, G.; Wang, F. Emerging Photoluminescence in Monolayer MoS₂. *Nano Lett.* **2010**, *10*, 1271–1275.
- Zeng, H. L.; Dai, J. F.; Yao, W.; Xiao, D.; Cui, X. D. Valley Polarization in MoS₂ Monolayers by Optical Pumping. *Nat. Nanotechnol.* **2012**, *7*, 490–493.
- Mak, K. F.; He, K. L.; Shan, J.; Heinz, T. F. Control of Valley Polarization in Monolayer MoS₂ by Optical Helicity. *Nat. Nanotechnol.* **2012**, *7*, 494–498.
- Lee, C.; Yan, H.; Brus, L. E.; Heinz, T. F.; Hone, J.; Ryu, S. Anomalous Lattice Vibrations of Single- and Few-Layer MoS₂. *ACS Nano* **2010**, *4*, 2695–2700.
- Radisavljevic, B.; Radenovic, A.; Brivio, J.; Giacometti, V.; Kis, A. Single-Layer MoS₂ Transistors. *Nat. Nanotechnol.* **2011**, *6*, 147–150.
- Liu, H.; Ye, P. D. MoS₂ Dual-Gate MOSFET with Atomic-Layer Deposited Al₂O₃ as Top-Gate Dielectric. *IEEE Electron Device Lett.* **2012**, *33*, 546–548.
- Wang, H.; Yu, L. L.; Lee, Y.-H.; Shi, Y. M.; Hsu, A.; Chin, M. L.; Li, L.-J.; Dubey, M.; Kong, J.; Palacios, T. Integrated Circuits Based on Bilayer MoS₂ Transistors. *Nano Lett.* **2012**, *12*, 4674–4680.
- He, K.; Poole, C.; Mak, K. F.; Shan, J. Experimental Demonstration of Continuous Electronic Structure Tuning via Strain in Atomically Thin MoS₂. *Nano Lett.* **2013**, DOI: 10.1021/nl4013166, and references therein.
- Bertolazzi, S.; Brivio, J.; Kis, A. Stretching and Breaking of Ultrathin MoS₂. *ACS Nano* **2011**, *5*, 9703–9709.
- Castellanos-Gomez, A.; Poot, M.; Steele, G. A.; van der Zant, H. S. J.; Agraït, N.; Rubio-Bollinger, G. Elastic Properties of Freely Suspended MoS₂ Nanosheets. *Adv. Mater.* **2012**, *24*, 772–775.
- Yasumura, K. Y.; Stowe, T. D.; Chow, E. M.; Pfafman, T.; Kenny, T. W.; Stipe, B. C.; Rugar, D. Quality Factors in Micron- and Submicron-Thick Cantilevers. *J. Microelectromech. Syst.* **1999**, *9*, 117–125.
- Yang, J. L.; Ono, T.; Esashi, M. Energy Dissipation in Submicrometer Thick Single-Crystal Silicon Cantilevers. *J. Microelectromech. Syst.* **2002**, *11*, 775–783.
- Southworth, D. R.; Craighead, H. G.; Parpia, J. M. Pressure Dependent Resonant Frequency of Micromechanical Drumhead Resonators. *Appl. Phys. Lett.* **2009**, *94*, 213506.
- Cross, M. C.; Lifshitz, R. Elastic Wave Transmission at an Abrupt Junction in a Thin Plate, with Application to Heat Transport and Vibrations in Mesoscopic Systems. *Phys. Rev. B* **2001**, *64*, 085324.
- Feng, X. L.; He, R.; Yang, P.; Roukes, M. L. Very High Frequency Silicon Nanowire Electromechanical Resonators. *Nano Lett.* **2007**, *7*, 1953–1959.
- Wah, T. Vibration of Circular Plates. *J. Acoust. Soc. Am.* **1962**, *34*, 275–281.
- Suzuki, H.; Yamaguchi, N.; Izumi, H. Theoretical and Experimental Studies on the Resonance Frequencies of a Stretched Circular Plate: Application to Japanese Drum Diaphragms. *Acoust. Sci. Technol.* **2009**, *30*, 348–354.
- Postma, H. W. C.; Kozinsky, I.; Husain, A.; Roukes, M. L. Dynamic Range of Nanotube- and Nanowire-Based Electromechanical Systems. *Appl. Phys. Lett.* **2005**, *86*, 223105.
- Feng, X. L.; White, C. J.; Hajimiri, A.; Roukes, M. L. A Self-Sustaining Ultrahigh-Frequency Nanoelectromechanical Oscillator. *Nat. Nanotechnol.* **2008**, *3*, 342–346.
- Poggio, M.; Degen, C. L.; Mamin, H. J.; Rugar, D. Feedback Cooling of a Cantilever's Fundamental Mode below 5mK. *Phys. Phys. Lett.* **2007**, *99*, 017201.
- Thompson, J. D.; Zwickl, B. M.; Jayich, A. M.; Marquardt, F.; Girvin, S. M.; Harris, J. G. E. Strong Dispersive Coupling of a High-Finesse Cavity to a Micromechanical Membrane. *Nature* **2008**, *452*, 72–75.
- Sundaram, R. S.; Engel, M.; Lombardo, A.; Krupke, R.; Ferrari, A. C.; Avouris, Ph.; Steiner, M. Electroluminescence in Single Layer MoS₂. *Nano Lett.* **2013**, 1310.1021/nl400516a.
- Rabl, P.; Kolkowitz, S. J.; Koppens, F. H. L.; Harris, J. G. E.; Zoller, P.; Lukin, M. D. A Quantum Spin Transducer Based on Nanoelectromechanical Resonator Arrays. *Nat. Phys.* **2010**, *6*, 602–608.
- Karabacak, D.; Kouh, T.; Ekinci, K. L. Analysis of Optical Interferometric Displacement Detection in Nanoelectromechanical Systems. *J. Appl. Phys.* **2005**, *98*, 124309.
- Karabalin, R. K.; Matheny, M. H.; Feng, X. L.; Defay, E.; Le Rhun, G.; Marcoux, C.; Hentz, S.; Andreucci, P.; Roukes, M. L. Piezoelectric Nanoelectromechanical Resonators Based on Aluminum Nitride Thin Films. *Appl. Phys. Lett.* **2009**, *95*, 103111.
- Hiebert, W. K.; Vick, D.; Sauer, V.; Freeman, M. R. Optical Interferometric Displacement Calibration and Thermomechanical Noise Detection in Bulk Focused Ion Beam-Fabricated Nanoelectromechanical Systems. *J. Microeng. Microeng.* **2010**, *20*, 115038.

High Frequency MoS₂ Nanomechanical Resonators

Jaesung Lee^{1†}, Zenghui Wang^{1†}, Keliang He², Jie Shan², Philip X.-L. Feng^{1,*}

¹*Department of Electrical Engineering & Computer Science, Case Western Reserve University,
10900 Euclid Avenue, Cleveland, OH 44106, USA*

²*Department of Physics, Case Western Reserve University,
10900 Euclid Avenue, Cleveland, OH 44106, USA*

Table of Contents

S1. Measurement of Nanomechanical Resonances	2
<i>S1.1. Optical Interferometry Measurement System</i>	<i>2</i>
<i>S1.2. Interferometric Motion Transduction</i>	<i>4</i>
<i>S1.3. Thermomechanical Resonance Measurement and Noise Analysis</i>	<i>6</i>
<i>S1.4. Calculation of the Effective Mass of the Resonator</i>	<i>9</i>
<i>S1.5. Effect of Device Thickness</i>	<i>10</i>
S2. AFM and Thickness Measurement	11
S3. Theoretical Analysis of Device Elastic Behavior and Frequency Scaling	12
S4. Measuring Device Temperature and Laser Heating Effect	14
S5. Measurement of Pressure Dependence	16
S6. List of All Devices and Their Parameters	18

*Corresponding Author. Email: philip.feng@case.edu. [†]Equally contributed authors.

S1. Measurement of Nanomechanical Resonances

S1.1. Optical Interferometry Measurement System

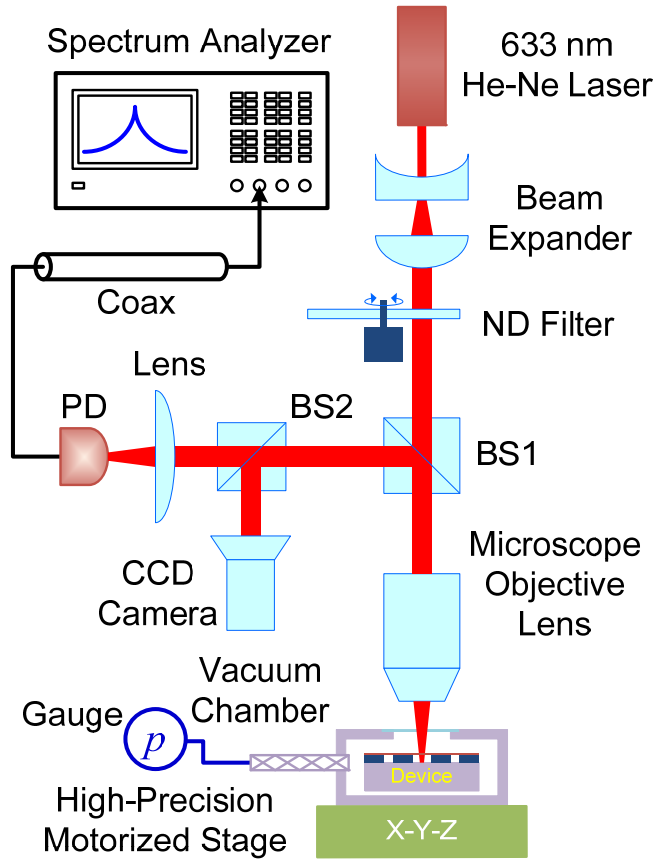


Figure S1. Schematic of the optical interferometry measurement system. The 632.8 nm beam from a He-Ne laser goes through a beam expander, followed by a neutral density (ND) filter. It is then focused onto the device through a 50× objective with window correction. The reflected beam, redirected by a beam splitter (BS1), is focused onto a photodetector (PD). The electronic signal is transmitted to a spectrum analyzer using a coaxial cable. The second beam splitter (BS2) and the CCD camera facilitate white light imaging. The device operates inside a vacuum chamber with a quartz window.

Figure S1 shows a schematic of the measurement system. Detection of the thermomechanical motion of the MoS₂ devices is based on optical interference from light waves reflected from the suspended MoS₂ diaphragm-vacuum interfaces, and from the vacuum-Si interface (described and

analyzed in more detail in Section S1.2). In this geometry, reflectivity of the bottom Si surface in the microtrench is important for achieving a large interferometry signal. Using buffered oxide etch (BOE) to remove the SiO₂ layer above, we obtain a smooth Si surface that is important for the interferometry. At the laser wavelength 632.8nm, the reflectivity of the Si surface is ~35%.

To achieve a tightly focused spot size on the device, the He-Ne laser beam is directed to a beam expander and then focused through a microscope objective (50×, NA=0.5) with optical window correction. This gives a spot size of ~1μm on the sample. To minimize laser heating, we limit the laser power on the device to be below ~700μW. Such laser power levels give good interferometric signals in resonance measurements, and do not induce observable frequency shift due to parasitic laser heating.

Optimizing the alignment of the optics is crucial for our measurements because of the minimal motions of the devices due to thermomechanical fluctuations. Position of the measured device is adjusted using a motorized stage (Prior Scientific ProScan III). The MoS₂ diaphragm's motion with respect to the underneath Si surface changes the interference and therefore leads to small-signal variations in the interferometric intensity. This is then detected with a low-noise photodetector (PD) (New Focus 1801), and recorded by an RF/microwave spectrum analyzer (Agilent E4440A). Most of the measurements are performed under moderate vacuum (~6mTorr) except for the pressure dependence measurements.

S1.2. Interferometric Motion Transduction

The reflectance R of the device (total reflected light intensity divided by incidence light intensity) is determined by the interference of the reflected light from all the interfaces. Analysis of the multiple reflections inside the device structure (Fig. S2 inset) gives¹

$$\frac{I_{\text{interferometry}}}{I_{\text{incident}}} = \left| \frac{r_1 e^{i(\phi_1 + \phi_2)} + r_2 e^{-i(\phi_1 - \phi_2)} + r_3 e^{-i(\phi_1 + \phi_2)} + r_1 r_2 r_3 e^{i(\phi_1 - \phi_2)}}{e^{i(\phi_1 + \phi_2)} + r_1 r_2 e^{-i(\phi_1 - \phi_2)} + r_1 r_3 e^{-i(\phi_1 + \phi_2)} + r_2 r_3 e^{i(\phi_1 - \phi_2)}} \right|^2. \quad (\text{S1})$$

Here, r_1 , r_2 and r_3 are reflection coefficients at the vacuum-MoS₂, MoS₂-vacuum, and vacuum-Si interface:

$$r_1 = \frac{n_{\text{vacuum}} - n_{\text{MoS}_2}}{n_{\text{vacuum}} + n_{\text{MoS}_2}}, \quad r_2 = \frac{n_{\text{MoS}_2} - n_{\text{vacuum}}}{n_{\text{MoS}_2} + n_{\text{vacuum}}}, \quad r_3 = \frac{n_{\text{vacuum}} - n_{\text{Si}}}{n_{\text{vacuum}} + n_{\text{Si}}}; \quad (\text{S2})$$

and ϕ_1 , ϕ_2 are the corresponding phase shifts:

$$\phi_1 = \frac{2\pi n_{\text{MoS}_2} d_1}{\lambda}, \quad \phi_2 = \frac{2\pi n_{\text{vacuum}} d_2}{\lambda}, \quad (\text{S3})$$

where d_1 is the MoS₂ thickness, d_2 is the vacuum gap depth, and λ is the laser wavelength.

Using Eqs. S1-S3, the reflectance R 's dependence on vacuum gap depth is calculated and plotted in Fig. S3 for $\lambda=632.8\text{nm}$ and $d_1=21\text{nm}$, as an example. We use $n_{\text{vacuum}}=1$, $n_{\text{MoS}_2}=5.263-1.140i$ and $n_{\text{Si}}=3.881-0.019i$. The dependence of R on d_1 is discussed in Section S1.5.

With no external drive, thermomechanical (Brownian) motions of the device lead to fluctuations of the vacuum gap size d_2 . These spatial fluctuations are transduced into the variations in R . Therefore, the slope at $d_2=290\text{nm}$ (the SiO₂ thickness) in Fig. S2 determines the “displacement-to-optical-reflectance” responsivity, and is estimated to be $-0.38\%/nm$.

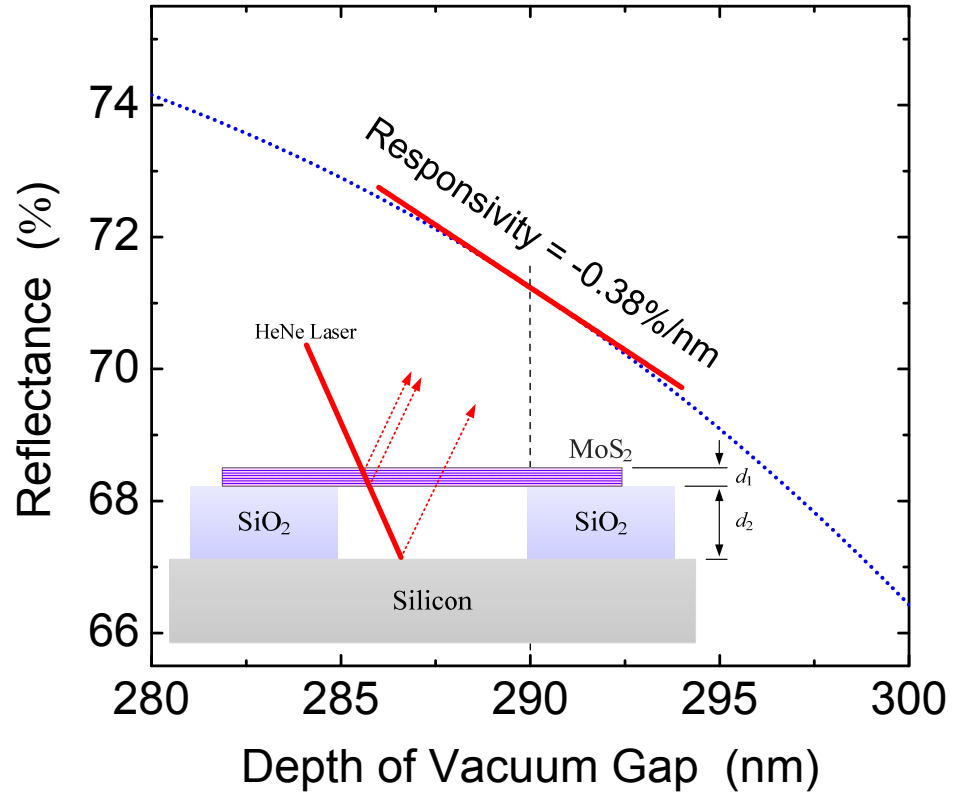


Figure S2. Optical reflectance of the device versus the vacuum gap size for $\lambda=632.8\text{nm}$ and $d_1=21\text{nm}$. The slope of the curve at 290nm (the vacuum gap size in our devices, indicated by the vertical dashed line) determines the responsivity of the system. *Inset:* Schematic of reflection at multiple interfaces. (Higher order reflections are not shown for clarity, but are included in the calculation).

S1.3. Thermomechanical Resonance Measurement and Noise Analysis

The signal measured on the spectrum analyzer typically takes the form of a resonance response on top of a frequency-dependent background (see Fig. S3, and also Fig. 1 and Fig. 2 in the main text for typical examples). To relate the measured electronic signal to the mechanical motion of the device, we perform analysis on the thermomechanical noise.

In the frequency domain, the thermomechanical motion of a resonator is given as³

$$S_{x,th}^{1/2}(\omega) = \left[\frac{4\omega_0 k_B T}{QM_{eff}} \cdot \frac{1}{(\omega_0^2 - \omega^2)^2 + (\omega_0 \omega / Q)^2} \right]^{\frac{1}{2}}, \quad (S4)$$

and when the device is on resonance, the expression simplifies to

$$S_{x,th}^{1/2}(\omega_0) = \sqrt{\frac{4k_B T Q}{\omega_0^3 M_{eff}}}. \quad (S5)$$

Here, k_B , T , ω_0 , Q , and M_{eff} are, respectively, the Boltzmann's constant, temperature, angular resonance frequency, quality factor, and the effective mass of the device (more details in Section S1.4). For example, for the 68.1nm-thick MoS₂ resonator in Fig. 1 left panel in the main text, using its dimensions, measured resonance frequency, measured Q , temperature (300K), and Eq. S5, we determine its thermomechanical displacement noise spectral density on resonance to be $S_{x,th}^{1/2} = 125.3 \text{ fm/Hz}^{1/2}$.

Assume the noise processes are uncorrelated, the total noise power spectral density (PSD) is the sum of the PSDs from individual noise processes. Thus we have $S_{v,total}^{1/2} = (S_{v,th} + S_{v,sys})^{1/2}$.

Here $S_{v,th}^{1/2}$ is the thermomechanical motion noise spectral density translated into the electronic domain, through the ‘displacement-to-voltage’ responsivity $\Re \equiv S_{v,th}^{1/2}/S_{x,th}^{1/2}$. The other term, $S_{v,sys}^{1/2}$, is the voltage noise floor of the measurement system, which depends on the details of the detection scheme. Typically we have $S_{v,sys}^{1/2} \approx 0.1\text{--}0.35 \mu\text{V/Hz}^{1/2}$ in the 10–60MHz frequency band, which slightly increases with increasing frequency. The level of $S_{v,sys}^{1/2}$ determines the off-resonance ‘baseline’ background ($S_{v,total}^{1/2} \approx S_{v,sys}^{1/2}$ off the resonance).

We fit our data to the expression for $S_{v,total}^{1/2}$, by using $S_{v,th}^{1/2} = \Re \times S_{x,th}^{1/2}$ and treating $S_{v,sys}^{1/2}$ as a frequency-dependent function:

$$S_{v,total}^{1/2} = \left(\Re^2 \times S_{x,th} + S_{v,sys} \right)^{1/2} = \sqrt{\Re^2 \left(\frac{4\omega_0 k_B T}{QM_{eff}} \cdot \frac{1}{(\omega_0^2 - \omega^2)^2 + (\omega_0 \omega / Q)^2} \right) + S_{v,sys}}. \quad (\text{S6})$$

From the fitting we obtain $S_{v,sys}^{1/2}$, Q , and \Re (assuming $T = 300\text{K}$).

Figure S3 (from the same device as in main text Fig. 1 left panel) shows an example of the fitting to the measured noise spectral density, with data (measured voltage spectral density, $S_{v,total}^{1/2}$) plotted against the left y-axis. We then convert voltage spectral density to displacement spectral density through the relationship $S_x^{1/2} = S_v^{1/2}/\Re$, with displacement scale displayed on the right y-axis. The displacement sensitivity of the measurement system is defined as $S_{x,sys}^{1/2} = S_{v,sys}^{1/2}/\Re$, the equivalent ‘fictitious’ displacement that would transduce into the actual electronic-domain noise floor of the measurement system. For example, the 68.1nm-thick MoS₂ resonator, from which the data is shown in Fig. S3, is a motion transducer with a displacement

sensitivity of $S_{x,sys}^{1/2} = 49.5 \text{ fm/Hz}^{1/2}$. From the plot one can directly tell that the responsivity of this system is $\mathfrak{R} = S_{v,sys}^{1/2} / S_{x,sys}^{1/2} = 0.117 \mu\text{V/Hz}^{1/2} / 0.0495 \text{ pm/Hz}^{1/2} = 2.36 \mu\text{V/pm}$. We note that MoS₂ devices with different thicknesses have different responsivities and sensitivities (see Section S1.5 for more details). For each of the MoS₂ devices, we have carefully performed similar signal transduction analysis as briefly discussed above and illustrated in Fig. S3.

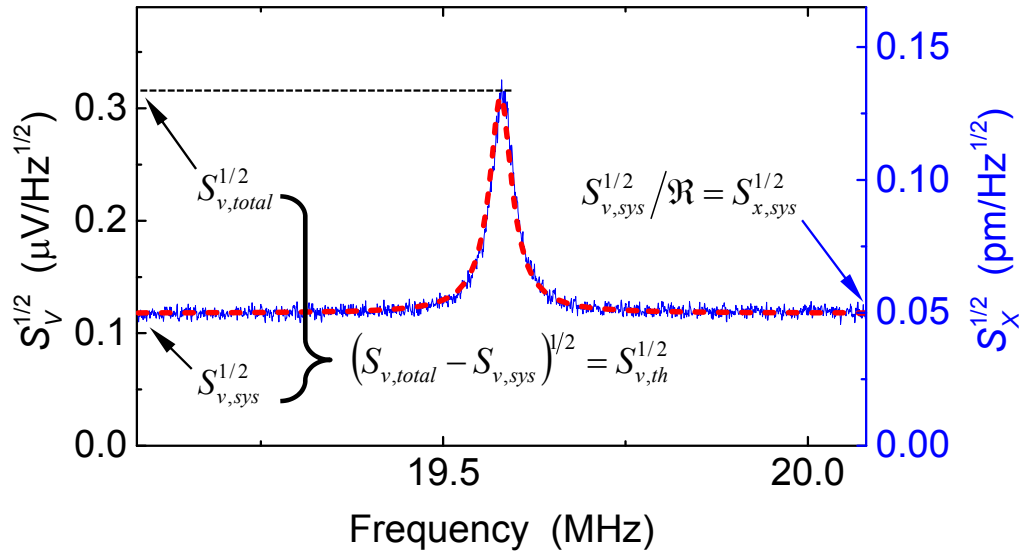


Figure S3. Example of measured thermomechanical resonance spectrum and analysis (from the same device as in main text Fig. 1 left panel). Annotations indicate how various quantities can be read off from the figure and are related to each other. See the text in Section S1.3 for more details.

S1.4. Calculation of the Effective Mass of the Resonator

In order to use Eq. S4 and S5 to estimate the amplitude of the Brownian motion, one needs to calculate the effective mass of the device, which depends on the mode shape of the resonance. Here we calculate the effective masses for a circular plate and a membrane in their fundamental flexural modes of out-of-plane vibrations. For a circular plate with clamped edge, the deflection for the lowest mode ($m=0$, $n=1$) as a function of the normalized radial position r ($0 \leq r \leq 1$) is given as⁴

$$Z_{01}(r) = J_0(\beta_{01} \cdot r) - \frac{J_0(\beta_{01})}{I_0(\beta_{01})} \cdot I_0(\beta_{01} \cdot r), \quad (S7)$$

where J_0 is the 0th-order Bessel function J , and I_0 is the 0th-order extended Bessel function I . For the fundamental mode, $\beta_{01}^2 = 10.216$. The normalized modal shape is defined as

$$u_{01}(r) = \frac{Z_{01}(r)}{\max(Z_{01})}, \quad (S8)$$

and the effective mass can be calculated as

$$M_{eff,01} = M \cdot \frac{1}{\pi} \int_0^1 2\pi r \cdot [u_{01}(r)]^2 dr. \quad (S9)$$

Here M is the total mass of the resonator. Using Eq. S9 we calculate the effective mass of a circular plate to be $M_{eff,01} = 0.1828M$ for the fundamental out-of-plane mode.

Similarly, for a circular membrane, the mode shape is

$$Z_{01}(r) = J_0(\beta_{01} \cdot r), \quad (\text{S10})$$

where $\beta_{01} = 2.405$. This yields an effective mass of $M_{\text{eff},01} = 0.2695M$.

S1.5. Effect of Device Thickness

We examine how the MoS₂ thickness affects the interferometry measurement. Using the same equations in section S1.2 (Eqs. S1-S3), the dependence of the device reflectance R on MoS₂ thickness is calculated and plotted in Fig. S4, illustrating how the “displacement-to-optical-reflectance” responsivity is modulated by the device thickness d_1 .

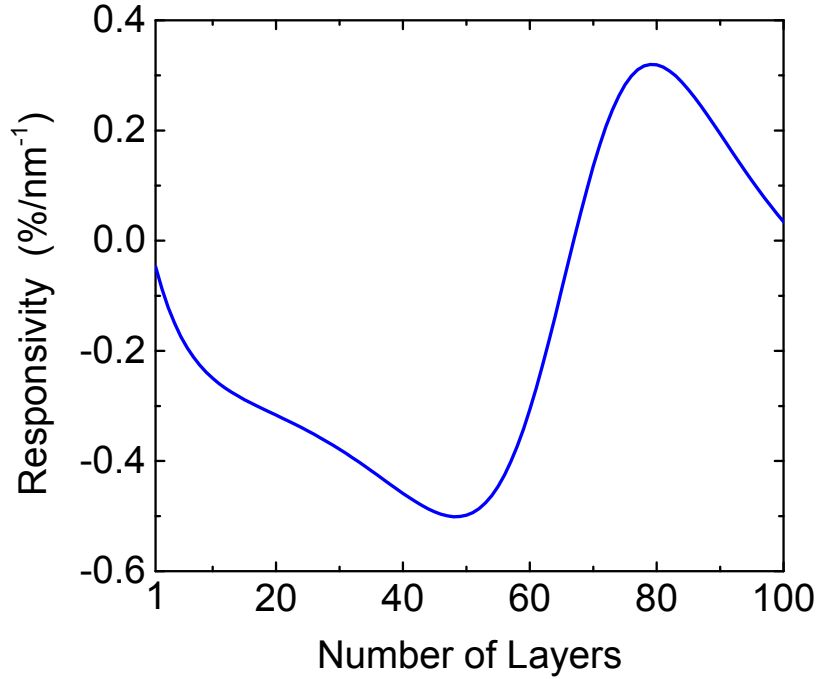


Figure S4. Calculated optical interferometric transduction responsivity as a function of MoS₂ thickness. Note that for certain thickness, the responsivity is 0.

S2. AFM and Thickness Measurement

We obtain AFM images and estimate thicknesses of our devices using an Agilent N9610A AFM. We start with coarse scans to locate the device and center it in the scan field, followed by slow scans with high resolution over the entire device area. We then take multiple traces across the edge of the flake in the resulting AFM data, and multiple measurements are made on each trace. The average value and standard deviation of the measured height differences are used as values for the thickness and its uncertainty. Figure S5 shows the AFM data from one of our thinnest devices (resonance shown in Fig. 2b of the main text).

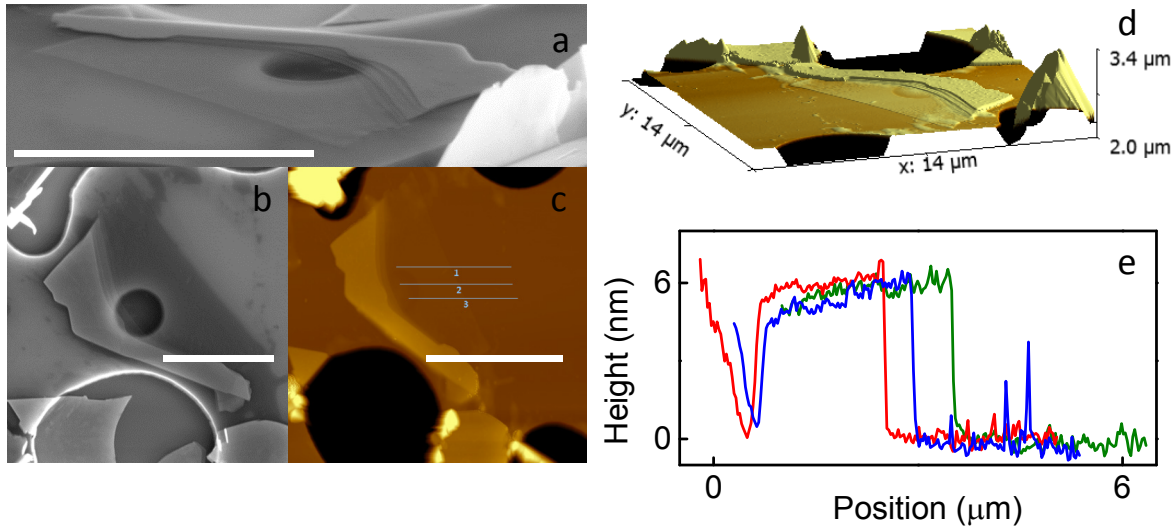


Figure S5. AFM and thickness measurement of our thinnest device ($t=6.1\pm0.2\text{nm}$). **a, b:** Perspective view and top view SEM images. **c:** AFM scan with lines indicating the position of the height traces. **d:** 3D AFM image. **e:** the height traces from the AFM scan. The green, blue and red lines correspond to trace 1, 2 and 3 in **c**, respectively. All scale bars: $5\mu\text{m}$.

S3. Theoretical Analysis of Device Elastic Behavior and Frequency Scaling

This section presents our theoretical analysis and modeling of the resonance frequency. For a circular disk with bending rigidity and non-zero tension, the resonance frequency is^{5,6}

$$\omega_{mn} = \left(k_2^{mn} \frac{d}{2} \right) \sqrt{\frac{16D}{\rho d^4} \left[\left(k_2^{mn} \frac{d}{2} \right)^2 + \frac{\gamma d^2}{4D} \right]}. \quad (\text{S11})$$

Here ω_{mn} is the angular frequency for the resonance mode (m, n) , d is the diameter of the disk, ρ is the areal (2D) mass density (kg/m²) of the material, γ is the tension (force per unit length, in N/m, as in surface tension) inside the disk. $D = E_Y t^3 / [12(1 - \nu^2)]$ is the bending rigidity, with E_Y being the Young's modulus, t the thickness of the disk, and ν the Poisson's ratio. k_2^{mn} is a mode-dependent parameter that is usually solved numerically.

In the limit of an ideal membrane in which tension dominates, $\gamma d^2 / D \rightarrow \infty$, Eq. S11 becomes

$$\omega_{mn} = \frac{(k_2^{mn} d)}{d} \sqrt{\frac{\gamma}{\rho}}, \quad (\text{S12})$$

which is the ‘membrane limit’ of resonance frequency dependence on geometry. Note that the formality of this equation may differ from the other forms of membrane equation, because we used surface tension γ (force per unit length, N/m), which is more meaningful for 2D structures, instead of other forms such as tension (force, in N) or stress (force per unit cross-sectional area, with units of Pa, N/m²) which are more applicable to 3D structures. As a result, the frequency depends on the thickness t through the dependence on ρ , the 2D mass density.

In the other limit where the bending rigidity dominates, $\gamma d^2 / D \rightarrow 0$, Eq. S11 approaches

$$\omega_{mn} = \frac{(k_2^{mn}d)^2}{d^2} \sqrt{\frac{D}{\rho}}, \quad (\text{S13})$$

which is the well-known equation for an ideal circular plate. Both limits are plotted as dashed lines in Fig. 4 of the main text.

In the regime where *neither* tension *nor* bending rigidity is negligible, $(k_2^{mn}d/2)$ can be approximated by the following analytical expression⁶

$$(k_2^{mn}d/2)^4 = \alpha + (\beta - \alpha)e^{[-\eta e^{\delta \ln(x)}]}, \quad (\text{S14})$$

where $x = \gamma d^2/(4D)$. For the fundamental-mode ($m=0, n=1$) resonance, the values of parameters α , β , η , δ are given in Ref. 6. It is also shown that the error between the numerical solution and the analytical approximation remains below 3.8% for this mode⁶.

Using this analytical approximation, we compute the fundamental-mode resonance frequency of clamped MoS₂ diaphragms with different diameters and thicknesses (see Fig. 4 main text). Here we use 5.06g/cm³ for the 3D mass density of MoS₂, and 0.7nm as the monolayer thickness^{7,8}. Poisson's ratio is chosen to be $\nu=0.165$, same as that of graphite in the basal plane⁹. Indeed, our results are not sensitive to the value of Poisson's ratio within a reasonable range: when a device is near the ideal membrane limit, Poisson's ratio has no effect on the resonance as it does not appear in the membrane equation; when it is in the plate limit, Poisson's ratio enter the equation through the bending rigidity D ,

$$\omega_{mn} \propto \sqrt{D} \propto \sqrt{\frac{1}{(1-\nu^2)}}. \quad (\text{S15})$$

If we use some other values from the literature, such as 0.25^{10} , 0.125^{11} , or 0.27^{12} , the resulting difference is always less than 2.5%.

We use Young's modulus of $E_Y=0.2\text{TPa}$ as suggested by existing works^{11,13,14,15,16}. The calculated results are consistent with our experimental data. In Fig. 4 of the main text, we show calculation for tension values ranging from 0.1–0.5N/m (except for $d=0.5\mu\text{m}$), as typically observed in exfoliated nanosheets^{13,14,15,17}. For the $0.5\mu\text{m}$ devices, we show an additional curve with a tension of 4.2N/m, which can lead to GHz MoS_2 resonators. This tension level corresponds to a strain of only 3% in monolayer and 1.5% in bilayer, still significantly below the intrinsic strain limit of this material^{13,16}.

S4. Measuring Device Temperature and Laser Heating Effect

Experimentally determining the temperature of a suspended MoS_2 device is particularly challenging, given the small dimensions and the configurations of our devices (*e.g.*, no electrical contacts or electrodes). Conventional thermometry techniques are not applicable. In this work, we exploit intrinsic properties of our devices and use the device itself as a thermometer. The specific technique we employ, called noise thermometry,^{3,18,19,20} uses the device's intrinsic thermomechanical noise spectrum to precisely determine its temperature, according to the fundamental equipartition theorem and statistical mechanics. This allows us to directly measure the device temperature with very good precision, through analyzing the noise spectrum of the device's thermomechanical motion, at a series of laser power levels. The device temperature is related to its thermomechanical motion amplitude by

$$T = \frac{k_{eff}}{2\pi k_B} \int_0^\infty S_{x,th}(\omega) d\omega. \quad (S16)$$

Here, k_{eff} is the effective spring constant of the resonator and k_B is the Boltzmann's constant. To use the measured voltage domain spectrum density, we use $S_{v,th}^{1/2} = \Re \times S_{x,th}^{1/2}$ (see Section S1.3):

$$T = \frac{k_{eff}}{2\pi k_B} \int_0^\infty \left(\frac{S_{v,th}^{1/2}(\omega)}{\Re} \right)^2 d\omega, \quad (S17)$$

where \Re is responsivity (displacement-to-voltage transduction gain) of the measurement setup, and can be calibrated experimentally.²¹

To examine the heating effects, we use different laser powers. Since \Re linearly depends on the incident laser power, we normalize our expression accordingly:

$$T = C \frac{k_{eff}}{2\pi k_B} \int_0^\infty \left(\frac{S_{v,th}^{1/2}(\omega)}{I} \right)^2 d\omega, \quad (S18)$$

where I is the incident laser power and C is a constant which remains the same for all laser power levels.

At very low incident laser power levels ($\sim 100\mu\text{W}$ to $\sim 700\mu\text{W}$), we repeatedly observe that the resonance characteristics (center frequency f_0 and Q) are stable and relatively constant (while we observe frequency shift at higher laser power levels). Our noise thermometry confirms that at these low laser power levels, the device temperature is near room temperature ($\sim 300\text{K}$). Figure S6 plots the temperature measured from thermomechanical noise thermometry using Eqs. S16-S18 for two different devices, demonstrating negligible laser heating effect when the incident laser power is below $\sim 700\mu\text{W}$.

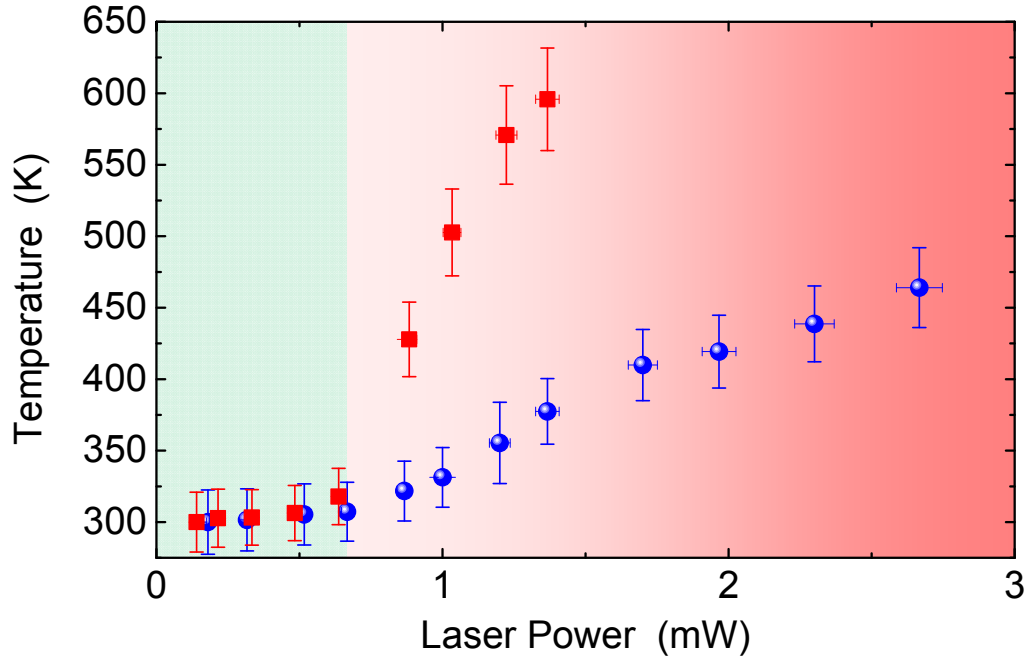


Figure S6. Measured device temperature under different levels of incident laser power. Data shown here have been taken from two different MoS₂ resonators. The green color zone indicates the region with negligible laser heating effect. Beyond this calibration, we have performed our resonance measurements for all the devices with laser power levels in the green zone.

S5. Measurement of Pressure Dependence

Most of the thermomechanical resonance measurements have been performed in moderate vacuum. In some similar structures made with graphene, bulging due to pressure difference caused by trapped air in the cavity has been observed²². We examine such effect in our MoS₂ device with SEM/AFM and resonance measurements.

In edge-clamped circular membrane with different pressure on different sides, the maximum deflection at the center is related to the pressure difference by²³

$$\Delta p = \frac{4tW_0}{a^2} \left(\frac{4}{3} \frac{t^2}{a^2} \frac{E_y}{1-\nu^2} + \frac{\gamma}{t} + \frac{64}{105} \frac{W_0^2}{a^2} \frac{E_y}{1-\nu^2} \right) \quad (\text{S19})$$

where Δp is the pressure difference, t is the thickness, γ is the initial tension (in N/m) in the membrane, a is the radius, E_y is Young's modulus, ν is Poisson's ratio, and W_0 is the deflection of membrane. Using our thinnest 1.9 μ m-diameter device (#20 in Table S1) as an example, we estimate the deflection under $\Delta p = 10^5$ Pa (using $\gamma = 0.3$ N/m) is 25 nm. From both SEM and AFM measurements we do not observe clear evidence confirming such bulging effect (Fig. S5). We have found the same behavior for all the devices we measured.

Furthermore, we have performed pressure dependence measurement on the thermomechanical resonances. If there were air volume trapped underneath the MoS₂ diaphragm, as the external pressure in the vacuum chamber goes down, we would have expected to observe the resonance frequency increases due to increasing tension induced by the growing pressure difference (Fig. S7, magenta dashed line), as seen in some graphene resonators with similar geometry¹⁸. However, we have not observed this trend in the measured resonance frequency of our devices based on MoS₂ diaphragms fully covering the microtrenches. Measured data from one such example is shown in Fig. S7 (blue circles in the middle). As shown, these devices behave the same way as the devices based on MoS₂ diaphragms incompletely covering the circular microtrench (data from an example device is shown in Fig. S7, red half-filled circles in the bottom), which should not experience any pressure difference. These results indicate that our MoS₂ resonators possibly do not experience any bulging and tensioning induced by sustained trapped air underneath the MoS₂ diaphragms.

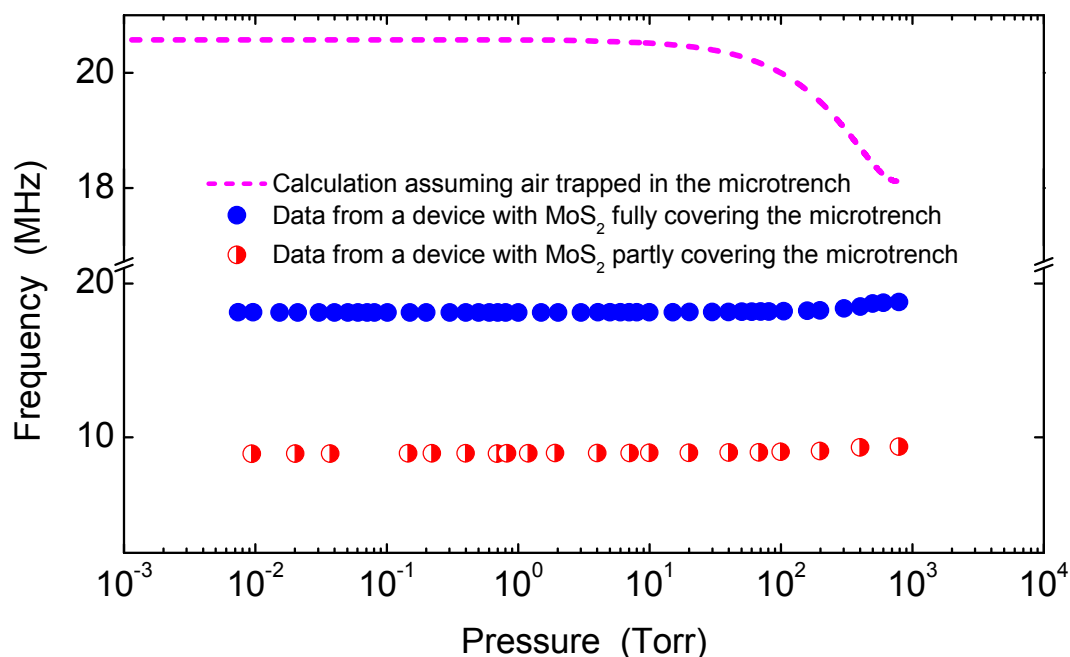


Figure S7. Measured pressure dependence of resonance frequency. *Dashed line:* theoretical calculation of the resonance frequency of a MoS₂ resonator with 1atm of air trapped underneath the MoS₂ diaphragm (using geometry from device #2 in Table S1). Note the curve is plotted on a separate scale than the experimental data for clarity. *Blue circles:* measured resonance frequency of such a device (#2 in Table S1). *Red half-filled circles:* measured data from a device where MoS₂ diaphragm partially covers the microtrench.

S6. List of All Devices and Their Parameters

Figure S8 reproduces Fig. 3a&b in the main text. Table S1 provides a list all the devices we have measured, with their specifications and parameters. Each device in Fig. S8 is indexed and labeled with a number, corresponding to the device number listed in Table S1.

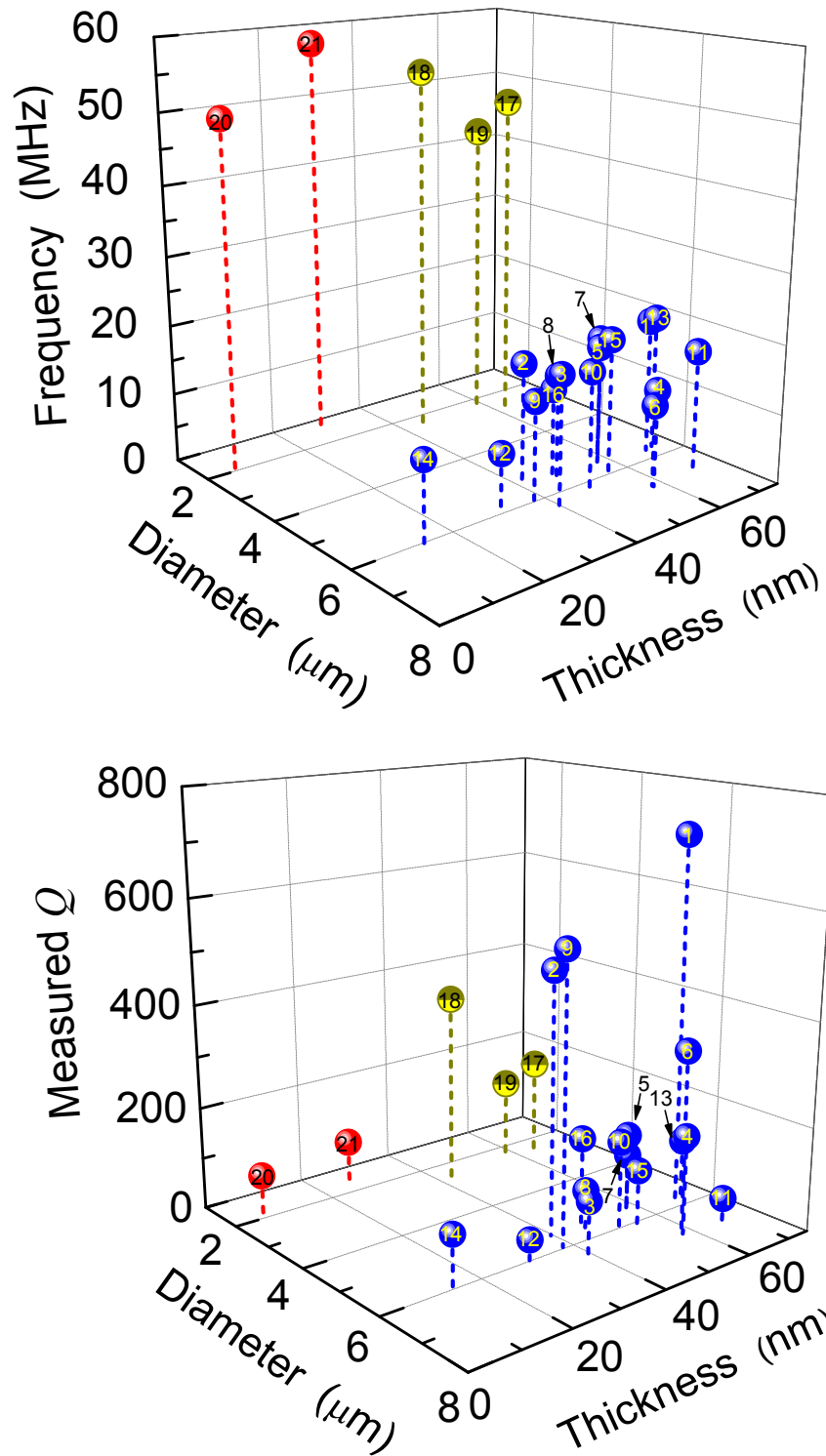


Figure S8. Measured resonance frequency and quality (Q) factors of all the devices. (These plots are reproductions of those in Fig. 3a&b in the main text, with all devices labeled).

Table S1 List of Devices and Their Parameters							
Device #	Diameter d (μm)	Thickness t (nm)	Resonance Frequency f_0 (MHz)	Quality Factor Q	$f_0 \times Q$ (MHz)	Displacement Sensitivity $S_{x,\text{sys}}^{1/2}$ (fm/Hz ^{1/2})	Comments
1	5.71	68.1±0.8	19.68	710	13900	49.5	Fig. 1, Left Panel
2	5.51	39.6±0.5	17.99	500	8995	91.7	
3	6.38	39.6±0.5	26.85	100	2685	171.9	
4	6.81	57.5±2.1	14.06	190	2671	30.2	
5	5.53	57.5±2.1	17.25	150	2588	39.9	
6	6.78	57.5±2.1	11.72	350	4102	31.4	
7	5.53	57.5±2.1	18.46	110	2031	32.2	
8	5.73	45.4±1.1	15.74	80	1259	84.9	
9	5.96	38.0±1.6	14.13	550	7772	33.5	Fig. 1, Right Panel
10	6.17	48.8±1.1	16.76	180	3017	90.8	
11	6.93	66.0±1.1	18.29	50	914.5	51.0	
12	5.99	30.3±0.3	8.49	40	340	41.4	
13	5.65	70.2±0.7	19.65	110	2162	43.6	
14	6.06	13.6±0.8	11.54	105	1212	99.4	
15	6.05	54.6±2.5	19.99	105	2099	69.5	
16	5.51	46.6±1.3	12.99	170	2208	41.3	
17*	2.69	62.2±0.7	48.10	200	9620	51.1	Fig. 2a
18*	2.41	57.5±2.1	43.77	160	7003	40.9	
19*	2.53	43.0±1.4	53.72	370	19880	49.5	Fig. 2c
20	1.90	6.1±0.7	49.70	80	4473	243.1	Fig. 2b
21	1.51	27.2±0.5	57.89	80	4921	205.1	Fig. 2d
* Device with less than complete coverage.							

References

- ¹ Blake, P., Hill, E.W., Castro Neto, A.H., Novoselov, K.S., Jiang, D., Yang, R., Booth, T.J. & Geim, A.K. Making Graphene Visible. *Appl. Phys. Lett.* **91**, 063124 (2007).
- ² Beal, A.R. & Hughes, H.P. Kramers-Krönig Analysis of the Reflectivity Spectra of 2H-MoS₂, 2H-MoSe₂ and 2H-MoTe₂. *J. Phys. C: Solid State Phys.* **12**, 881-890 (1979).
- ³ Cleland, A.N. *Foundations of Nanomechanics: from Solid-State Theory to Device Applications*. Springer, New York, 2003.
- ⁴ Graff, K.F. *Wave Motion in Elastic Solids*. Dover Publications, New York, 1991.
- ⁵ Wah, T. Vibration of Circular Plates. *J. Acoust. Soc. Am.* **34**, 275-281 (1962).
- ⁶ Suzuki, H., Yamaguchi, N. & Izumi, H. Theoretical and Experimental Studies on the Resonance Frequencies of a Stretched Circular Plate: Application to Japanese Drum Diaphragms. *Acoust. Sci. Technol.* **30**, 348–354 (2009).
- ⁷ Mak, K.F., Lee, C., Hone, J., Shan, J. & Heinz, T.F. Atomically Thin MoS₂: A New Direct-Gap Semiconductor. *Phys. Rev. Lett.* **105**, 136805 (2010).
- ⁸ Splendiani, A., Sun, L., Zhang Y., Li T., Kim, J., Chim, C.-Y., Galli, G. & Wang, F. Emerging Photoluminescence in Monolayer MoS₂. *Nano Lett.* **10**, 1271-1275 (2010).
- ⁹ Blakslee, O.L., Proctor, D.G., Seldin, E.J., Spence, G.B. & Weng, T. Elastic Constants of Compression-Annealed Pyrolytic Graphite. *J. Appl. Phys.* **41**, 3373-3382 (1970).
- ¹⁰ Yue, Q., Kang, J., Shao, Z., Zhang, X., Chang, S., Wang, G., Qin, S. & Li, J. Mechanical and Electronic Properties of Monolayer MoS₂ under Elastic Strain. *Phys. Lett. A* **376**, 1166-1170 (2012).
- ¹¹ Lovell, M.R., Khonsari, M.M. & Marangoni, R.D. A Finite Element Analysis of the Frictional Forces between a Cylindrical Bearing Element and MoS₂ Coated and Uncoated Surfaces. *Wear* **194**, 60-70 (1996).
- ¹² Feldman, J.L. Elastic Constants of 2H-MoS₂ and 2H-NbSe₂ Extracted from Measured Dispersion Curves and Linear Compressibilities. *J. Phys. Chem. Solids* **37**, 1141-1144 (1976).

-
- ¹³ Bertolazzi, S., Brivio, J. & Kis, A. Stretching and Breaking of Ultrathin MoS₂. *ACS Nano* **5**, 9703-9709 (2011).
- ¹⁴ Castellanos-Gomez, A., Poot M., Steele, G.A, van der Zant, H.S.J., Agraït, N. & Rubio-Bollinger, G. Mechanical Properties of Freely Suspended Semiconducting Graphene-Like Layers Based on MoS₂. *Nanoscale Res. Lett.* **7**, 233 (2012).
- ¹⁵ Castellanos-Gomez, A., Poot M., Steele, G.A, van der Zant, H.S.J., Agraït, N. & Rubio-Bollinger, G. Elastic Properties of Freely Suspended MoS₂ Nanosheets. *Adv. Mater.* **24**, 772-775 (2012).
- ¹⁶ Li, T. Ideal Strength and Phonon Instability in Single-Layer MoS₂. *Phys. Rev. B* **85**, 235407 (2012).
- ¹⁷ Lee, C., Wei, X., Kysar, J. W. & Hone, J. Measurement of the Elastic Properties and Intrinsic Strength of Monolayer Graphene. *Science* **321**, 385-388 (2008).
- ¹⁸ Bleszynski-Jayich, A.C., Shanks, W.E. & Harris, J.G.E. Noise Thermometry and Electron Thermometry of a Sample-on-Cantilever System below 1 Kelvin. *Appl. Phys. Lett.* **92**, 013123 (2008).
- ¹⁹ Montinaro, M., Mehlin, A., Solanki, H.S., Peddibhotla, P., Mack, S. & Awschalom, D.D. Feedback Cooling of Cantilever Motion Using a Quantum Point Contact Transducer. *Appl. Phys. Lett.* **101**, 133104 (2012).
- ²⁰ Poggio, M., Degen, C.L., Mamin, H.J. & Rugar, D. Feedback Cooling of a Cantilever's Fundamental Mode below 5 mK. *Phys. Rev. Lett.* **99**, 017201 (2007).
- ²¹ Hiebert, W.K., Vick, D., Sauer, V. & Freeman, M.R. Optical Interferometric Displacement Calibration and Thermomechanical Noise Detection in Bulk Focused Ion Beam-Fabricated Nanoelectromechanical Systems. *J. Micromech. Microeng.* **20**, 115038 (2010).
- ²² Bunch, J.S., Verbridge, S.S., Alden, J.S., van der Zande, A.M., Parpia, J.M., Craighead, H.G. & McEuen, P.L. Impermeable Atomic Membranes from Graphene Sheets. *Nano Lett.* **8**, 2458-2462 (2008).
- ²³ Schomburg, W. K. *Introduction to Microsystem Design*. Springer, 2011.